

Physen-Noise2Noise: Physics-Guided Self-Supervised Defocus Deblurring with Bias Correction under Low-Light Conditions

Ziyan Huang, Lang Wu, Hongji Wang, Yifei Liu, Dongliang Tang*, and Hongqiao Wang*

Abstract—Low-light, long-exposure defocus deblurring remains a challenging problem due to the simultaneous presence of severe blur and complex biased noise. Existing methods typically rely on simplified noise assumptions, which limits their effectiveness under realistic imaging conditions. In this work, we propose Physen-Noise2Noise, a self-supervised deblurring framework guided by the physical model of defocus imaging, which leverages noisy multi-frame observations without requiring clean reference images. Unlike conventional Noise2Noise-based approaches that assume zero-mean noise, we derive a frequency-domain constraint inherent to the defocus imaging process and incorporate it into the learning framework via a learnable noise bias parameter. In addition, a multi-frame noisy initialization strategy is introduced to suppress complex biased noise prior to deblurring, providing a more stable starting point for reconstruction. This formulation explicitly models biased noise and enables joint bias correction and high-frequency detail recovery during training. Furthermore, we develop a pretrain–finetune variant to enhance robustness and generalization under challenging noise conditions. Extensive experiments on both simulation and real-world datasets demonstrate that the proposed method consistently outperforms state-of-the-art self-supervised approaches for defocus deblurring in the presence of complex biased noise.

Index Terms—Complex biased noise, Defocus deblurring, Low-light imaging, Self-supervised learning.

I. INTRODUCTION

Defocus blur is a common degradation in practical imaging systems and can be formulated as an inverse problem in computational imaging, where the observed image is modeled as the convolution of a latent sharp image with a defocus point spread function (PSF), often further corrupted by noise. This degradation arises from mismatches between the sensor plane and the focal plane due to autofocus errors, depth variations, or inherent optical limitations, leading to significant loss of high-frequency details and degraded visual quality.

In many real-world low-light imaging applications, such as surveillance monitoring [1], microscopy [2], and Industrial Vision [3], defocus blur can coexist with complex biased noise. Under low-light conditions, the limited photon budget often necessitate long exposure times to achieve sufficient

signal levels. These strategies inevitably introduce a mixture of noise sources [4]–[6], including shot noise, dark current noise, thermal noise, and fixed-pattern noise. Moreover, the subsequent in-camera processing pipeline introduces additional spatial correlations [7]–[10], further deviating the noise characteristics from idealized spatially independent and zero-mean assumptions commonly adopted in conventional deblurring models. The interplay between defocus blur and noise further complicates the image degradation process and exacerbates the difficulty of deblurring. Therefore, designing high-quality defocus deblurring methods specifically tailored for low-light, long-exposure environments is of both considerable research significance and practical value.

While numerous deblurring algorithms excel under well-lit conditions [11]–[22], they falter in low-light environments. They struggle to distinguish genuine high-frequency edges from noise-induced perturbations, often resulting in either severe artifacts or over-smoothing. This limitation stems from insufficient exploration of the frequency-domain constraints inherent to defocus blur and the complex statistical properties of real-world noise. Recent self-supervised approaches like SSI [23] assume zero-mean, independent noise, failing with biased noise; UNID [24] lacks explicit noise modeling; and RLSN2N [2], despite combining Richardson-Lucy with Noise2Noise, is constrained by its handling of correlated noise and does not address bias. These observations reveals a fundamental challenge in defocus deblurring under low-light conditions: the mismatch between the deterministic forward degradation model and the complex, biased and spatially correlated noise encountered in real imaging systems. Existing methods typically rely on simplified assumptions such as zero-mean or independent noise, which are frequently violated in practice, leading to degraded restoration quality. As a result, it remains challenging to effectively integrate physical priors with realistic noise statistics in a self-supervised setting.

Typically, the noise between adjacent frames is independent and identically distributed [25], and its bias remains invariant over a short sequence of frames [26]. This property suggests that we can leverage multi-frame collaboration for preliminary denoising. On the other hand, defocus blur is essentially a low-pass filtering process that applies a deterministic attenuation to high-frequency components in the frequency domain, while observational noise perturbs these already attenuated components. This contradiction indicates that the core of image deblurring lies not in preemptive perfect denoising,

Ziyan Huang, Hongji Wang, Yifei Liu, and Hongqiao Wang are with the School of Mathematics and Statistics, Central South University, Changsha, 410083, People’s Republic of China (e-mail: 242111091@csu.edu.cn; 18707976263@163.com; 31250181@csu.edu.cn; hongqiao.wang@csu.edu.cn).

Lang Wu and Dongliang Tang are with the Key Laboratory for Micro/Nano Optoelectronic Devices of Ministry of Education, Hunan Provincial Key Laboratory of Low-Dimensional Structural Physics and Devices, School of Physics and Electronics, Hunan University, Changsha 410082, People’s Republic of China (e-mail: langwu@hnu.edu.cn; dltang@hnu.edu.cn).

but in leveraging the adversarial relationship between “high-frequency attenuation” and “high-frequency disturbance” during the restoration process. This insight leads us to consider an iterative guidance mechanism that progressively corrects noise bias, thereby suppressing artifacts induced by complex biased noise.

This work addresses defocus deblurring under low-light, long-exposure conditions. We propose a self-supervised deep learning framework, Physen-Noise2Noise (PN2N), which requires no clean reference images and incorporates the physical forward model of defocus blur into the optimization process while exploiting multi-frame observations for deblurring. Guided by the validated high-frequency attenuation constraint of defocus blur, the method first initializes the latent image using multiple noisy observations and then introduces a learnable bias parameter during reconstruction to adaptively correct biased noise. The main contributions of this work are summarized as follows:

- We analyze the frequency-domain constraint of defocus blur, particularly high-frequency attenuation, and introduce a learnable bias to model biased noise, enabling adaptive correction of noise expectation for improved restoration.
- We propose a self-supervised framework that requires no clean references, leveraging multi-frame observations and embedding the defocus forward model into optimization to achieve effective deblurring under low-light, long-exposure conditions.
- The proposed method delivers robust and high-quality deblurring under complex biased noise with minimal prior assumptions, maintaining stable performance in challenging real-world scenarios.

II. RELATED WORKS

A. Nonblind image deblurring

Wiener deconvolution (WD) [27] and the Richardson–Lucy algorithm (LRA) [28], [29] are classical deblurring methods that remain widely used today. NLR (nonlinear reconstruction) [30], built on the Richardson–Lucy framework, introduces two tunable parameters to apply nonlinear amplitude weighting, achieving improved performance. However, Wiener filtering assumes prior knowledge of the signal and noise power spectra, while LRA and NLR assume a Poisson noise model. When applied to genuinely blurred images, this model mismatch often produces artifacts or excessive smoothing, degrading perceptual quality.

Unlike traditional approaches, deep learning–based methods have recently made remarkable progress in image deblurring. Several works [24], [31]–[34] follow an autoregressive learning paradigm: the network output is convolved with the defocus PSF and compared to the observed blurred image to compute the loss, yielding promising results without paired training data. Other approaches also contribute to the area: Deep Image Prior (DIP)-based methods [35], [36] exploit network architecture as an implicit regularizer, while techniques such as denoising the deblurring result [2], [37] offer

alternative solutions. Nevertheless, these methods are generally outperformed by autoregressive approaches. Additionally, other research that relies on external resources, such as using CycleGAN for domain translation [38], is not fully self-supervised.

Nonblind deblurring under noisy conditions Wiener deconvolution [27], the Richardson–Lucy algorithm [28], [29], and nonlinear reconstruction [30] enhance robustness to noise by incorporating explicit noise models into the image formation process. In contrast, SSI [23], inspired by Noise2Void [39], adopts a mask-based learning strategy to achieve robustness; however, it relies on assumptions of spatially independent and unbiased noise. UNID [24] and [34] employ Monte Carlo Dropout [40] to improve robustness under relatively mild noise conditions. Nevertheless, the lack of explicit noise modeling limits their performance in more severe scenarios. RLSN2N [2] combines the classical Richardson–Lucy algorithm [28], [29] with the Noise2Noise paradigm [41], decomposing the restoration process into separate denoising and deblurring stages. However, it does not explicitly exploit the frequency-domain relationship between the noise distribution and the blurring process.

B. Image denoising

Traditional denoising methods include filtering [42], [43], transform domain techniques [44], [45], and total variation [46]. However, many of these approaches suffer from high computational complexity and tend to damage local image details. In recent years, deep learning-based methods have come to dominate the field of image denoising due to their superior performance [47]–[49]. Among them, supervised approaches [11]–[14] train neural networks in a supervised manner and have achieved state-of-the-art results. However, these methods require extensive pairs of clean and noisy images for training, a process that is both time-consuming and labor-intensive.

To alleviate this issue, a growing trend has emerged toward self-supervised denoising methods [50]. A representative work is Noise2Noise (N2N) [41], which recovers clean images from pairs of noisy images by learning to map one noisy observation to another under the assumption that the noise is zero-mean. However, N2N requires multiple noisy images, which limits its applicability. To overcome this limitation, one line of research, such as recorruped-to-recorruped [51] and generalized recorruped-to-recorruped [52], simulates training pairs by decomposing a single image but requires specifying the noise model and its parameters. Another line, including Noise2Void [39], Noise2Self [53], Neighbor2Neighbor [53], and Self2Self [54], leverages image spatial correlations to work with only a single image but introduces the additional assumption that noise is spatially independent. More recent works, such as Self-inspired Noise2Noise (SN2N) [2] and Pixel2Pixel [55], relax the assumption of spatial independence while retaining the assumption of unbiased noise. DeepDeWedge [25] constructs noise pairs from adjacent frames for training, thereby overcoming the data requirement of N2N, but does not account for the impact of biased noise.

III. METHODS

A. Degradation model

In defocus blur, light rays from a point source do not converge to a single point but instead form a disk, known as the circle of confusion, rather than a single point on the sensor. The point spread function (PSF) characterizes the impulse response of the imaging system to a point source. In many practical imaging scenarios, particularly under relatively small aperture settings where the depth of field is large, the defocus blur can be reasonably approximated as spatially invariant. Under this commonly adopted assumption, the degraded imaging process is formulated as a convolution between the sharp image x and the PSF:

$$y = PSF \otimes x + n, \quad (1)$$

where y denotes the blurred image, \otimes represents the convolution operator, $PSF \otimes x$ models the process of light propagation, and n accounts for the additive noise, which typically exhibits a complex biased distribution [4]–[6]. This reconstruction is typically formulated as an optimization problem:

$$\hat{x} = \arg \min_x \|PSF \otimes x - y\|_2^2. \quad (2)$$

This ill-posed inverse problem presents significant challenges: even minor noise can lead to substantial artifacts in the reconstructed image due to the inherent instability of the solution. These challenges underscore the critical need for defocus deblurring algorithms capable of operating in complex biased noise distributions.

B. Frequency domain constraint for defocus blur

Defocus blurring is characterized by the degradation model $PSF \otimes x$, which maps object images to blurred observations. This model inherently imposes a frequency domain constraint on the observations: the PSF governed by frequency domain physical laws produces characteristic blurring effects. Consequently, outputs from a defocus imaging system adhere to this constraint and cannot exhibit arbitrary variations. Although this phenomenon has been observed in prior works [56], [57], its mathematical implications have not been fully characterized. In this work, we aim to provide a formal analysis of this inherent structural property.

We employ continuous models for theoretical analysis, which can clearly reveal the frequency-domain characteristics of PSF convolution operators and the mechanisms of information loss, thereby providing theoretical guidance for practical operations in the discrete domain.

The full image space is denoted as \mathcal{I} , and the observed blurred image space \mathcal{V} is a subspace of \mathcal{I} . We do not impose additional constraints on the object images and assume that the object space \mathcal{O} coincides with the entire image space \mathcal{I} , i.e., any image in \mathcal{I} is treated as a feasible object image. The PSF acts as a mapping operator from \mathcal{O} to \mathcal{V} , which suppresses high-frequency details in the object image, resulting in blurred observations. According to Fourier optics theory [58] and

previous works [24], [59], [60], the above phenomenon occurs because the amplitude of the PSF's frequency response decays or vanishes in high-frequency regions. Based on this, we abstract the properties of the PSF commonly encountered in real-world scenarios into the following mathematical form:

Definition 1 (PSF Addressed in This Work). *Let F_p denote the Fourier transform of the PSF, where $\omega = (u, v)$ is the frequency vector with horizontal and vertical components u and v , respectively. The domain of ω is given by*

$$\omega \in \Omega = \mathbb{R} \times \mathbb{R}, \quad (3)$$

where Ω denotes the domain of the frequency vectors with horizontal and vertical components. Then it must satisfy one of the following conditions:

- 1) $\exists \omega_0 \in \Omega, |F_p(\omega_0)| = 0;$
- 2) $\forall \omega \in \Omega, |F_p(\omega)| > 0,$ and

$$\lim_{|\omega| \rightarrow \infty} |F_p(\omega)| = 0. \quad (4)$$

The following proposition elucidates how the observed image is controlled by the PSF, revealing the naturalness constraint. A brief proof is provided below, with full details available in the appendix.

We first analyze the theory under noise-free conditions.

Proposition 1. *Under the given PSF, the observed image space \mathcal{V} is a proper subspace of the full image space \mathcal{I} .*

Proof. According to the imaging model $PSF \otimes x$, \mathcal{V} is also a subspace of the object image space \mathcal{O} . \mathcal{O} and \mathcal{I} are energy-limited (finite energy in the frequency domain) because of physical constraints. It implies:

$$\forall x \in \mathcal{I}, \int_{\Omega} |F_x(\omega)|^2 d\omega < \infty, \quad (5)$$

where $F_x(\omega)$ is the Fourier transform of the x in \mathcal{I} .

Scenario 1 Assume the PSF satisfies condition (1), and let \mathcal{V} be a subspace of the image space \mathcal{I} . Since the PSF satisfies condition (1), there exists at least one frequency component ξ such that $|F_p(\xi)| = 0$.

Therefore, the Fourier transform of every element in \mathcal{V} is zero at ξ . Consider an element $i \in \mathcal{I}$. Its Fourier transform $F_i(\omega)$ satisfies $|F_i(\xi)| \neq 0$, implying that $i \notin \mathcal{V}$. Consequently, there exists an element $i \in \mathcal{I}$ such that $i \notin \mathcal{V}$, which establishes that \mathcal{V} is a proper subspace of \mathcal{I} .

Scenario 2 The second scenario is when the PSF follows the condition (2). Since the PSF exhibits high-frequency decay, $F_p(\omega)$ satisfies Eq. (4).

We now proceed to demonstrate that \mathcal{V} constitutes a proper subspace of \mathcal{I} . To ensure \mathcal{I} is certainly energy-limited as Eq. (5), the following must hold:

$$\forall y \in \mathcal{I}, \int_{\Omega} \left(\frac{|F_y(\omega)|^2}{|F_p(\omega)|^2} \right) d\omega = \int_{\Omega} |F_x(\omega)|^2 d\omega < \infty. \quad (6)$$

Taking $F_y(\omega)$ as:

$$F_y(\omega) = \frac{F_p(\omega)}{1 + |\omega|}, \quad (7)$$

since the PSF is also an image (i.e. $PSF \in \mathcal{I}$), it satisfies Eq. (5). Then $F_y(\omega)$ obeys:

$$\int_{\Omega} |F_y(\omega)|^2 d\omega \leq \int_{\Omega} |F_p(\omega)|^2 d\omega < \infty. \quad (8)$$

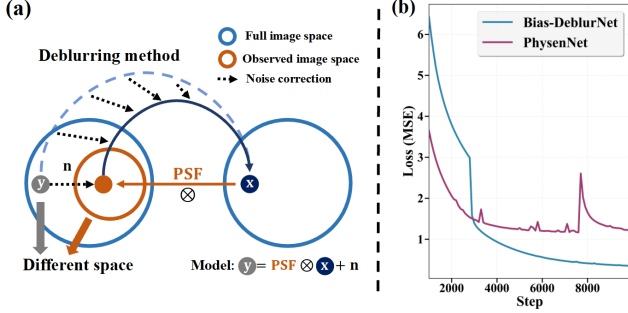


Fig. 1. (a) Impact of the defocus blur frequency constraint on deblurring. (b) A representative example of loss descent curves, comparing our joint optimization of deblurring and noise bias removal against conventional deblurring-only optimization. PhysenNet [61] is a method based on Eq. (2).

Therefore, $x \in \mathcal{I}$ and $F_p(\omega)$ follows condition (2), but lead to:

$$\int_{\Omega} \left(\frac{|F_y(\omega)|^2}{|F_p(\omega)|^2} \right) d\omega = \int_{\Omega} \frac{1}{(1+|\omega|)^2} d\omega = \infty, \quad (9)$$

so that $y \notin \mathcal{V}$. Consequently, there exists an element $i \in \mathcal{I}$ such that $i \notin \mathcal{V}$, which establishes that \mathcal{V} is a proper subspace of \mathcal{I} .

In summary, the observed image space \mathcal{V} is a proper subspace of the full image space \mathcal{I} :

$$\mathcal{V} \subsetneq \mathcal{I} = \mathcal{O}. \quad (10)$$

□

Proposition (1) indicates that not every image can be regarded as an observation obtained through a given PSF. And it reveals that the high-frequency domain of the observed image must satisfy the high-frequency constraint imposed by the PSF. In real-world scenarios, The observed image y is often corrupted by complex biased noise, which disrupts the original distribution of high-frequency components and thereby violates Eq. (6). As a result, y consistently lies outside the space of \mathcal{V} , implying that for any x in \mathcal{O} , the following holds:

$$y \neq PSF \otimes x. \quad (11)$$

This conclusion provides a crucial foundation for subsequent deblurring algorithm design. As illustrated in Fig. 1(a), if one attempts to perform deblurring via Eq. (2), the presence of Eq. (11) ensures that the loss is lower-bounded and cannot decrease below a certain value. By incorporating noise correction into the deblurring process for noisy blurred images, a high loss actively promotes noise correction, which in turn facilitates optimization toward improved deblurring performance, as shown in Fig. 1(b).

C. Multi-frame initial denoising

The proposed PN2N framework uses a two-step approach to solve this problem. It first leverages multi-frame noisy images for initial denoising and subsequently introduces a bias-adaptive physics-guided deep learning method to achieve noise bias removal and defocus deblurring. Specifically, the Self-inspired Noise2Noise (SN2N) method [2] is adopted for initialization.

Noise2Noise (N2N) [41] restores images using only pairs of noisy observations without requiring clean references. It relies on the assumption that the noise in different observations of the same signal is independent and identically distributed (*i.i.d.*) with zero mean. Under this assumption, minimizing the mean squared error between noisy image pairs drives the network to estimate the expectation of the underlying clean signal. The SN2N further improves robustness by enforcing prediction consistency between different noisy observations, as shown in Fig. 2(a). Given two noisy images (y_1, y_2) from the same latent signal, the network f_{θ} is trained with

$$\mathcal{L} = \mathbb{E}_{(y_1, y_2)} \left[|f_{\theta}(y_1) - y_2|_2^2 + |f_{\theta}(y_2) - y_1|_2^2 + \lambda_1 |f_{\theta}(y_1) - f_{\theta}(y_2)|_2^2 \right], \quad (12)$$

where λ_1 is a weighting coefficient. The first two terms follow the N2N, while the consistency term encourages identical predictions for different noisy observations of the same signal.

By splitting the multi-frame sequence into odd/even subsets, we can construct paired training samples [25]. When the noise distribution is unbiased (i.e., zero-mean), the SN2N initialization enables a direct mapping from noisy blurred observations to the corresponding clean observations. However, under low-light and long-exposure conditions, the noise distribution becomes biased, the observed blurred images will be mapped to

$$y' = PSF \otimes x + \mu, \quad (13)$$

where y' represents the denoised image obtained from y via SN2N, and μ denotes the expectation of the noise distribution to which n belongs, irregularly disrupting the distribution of high-frequency components in y' , which causes y' to lie outside the observed image space as shown in Fig. 1(a). When solving for \hat{x} on such an image y' , the result $PSF \otimes \hat{x}$ lies in the observed image space. Since y' itself still lies outside the space, there exists no \hat{x} that can reduce the loss $|PSF \otimes \hat{x} - y'|_2^2$ to zero, thus leading to optimization stagnation, as referred to in Section III-B.

This observation reveals a fundamental limitation of existing self-supervised denoising-based pipelines: the bias in the denoised result violates the physical consistency required by the forward model, preventing effective optimization in subsequent deblurring. Notably, this inconsistency manifests as optimization stagnation, which provides a valuable cue for estimating the underlying noise expectation μ . This insight motivates a joint formulation that explicitly accounts for noise bias during reconstruction.

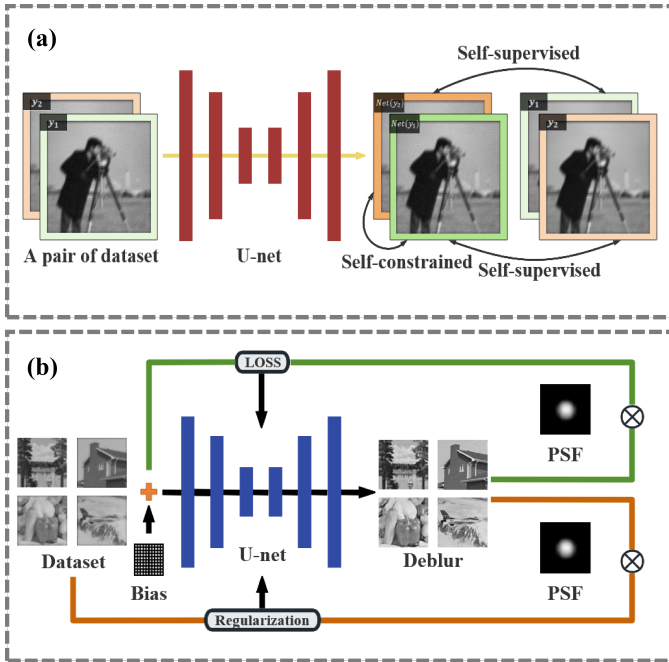


Fig. 2. (a) The SN2N strategy: integration of noise-to-noise loss and self-constrained loss. (b) Bias-DeblurNet architecture: design of its loss function and regularization. The original images used in this figure are from [62], [63].

D. Bias-adaptive physics-guided deblurring

We propose a bias-adaptive physics-guided deblurring network as step 2, termed Bias-DeblurNet, as illustrated in Fig. 2(b). It introduces a learnable parameter b to estimate the noise expectation and jointly optimize it with the network parameters:

$$R_{\theta}, b = \arg \min_{\theta, b} \mathbb{E}_{y'} \left[\|PSF \otimes R_{\theta}(y' - b) - (y' - b)\|_2^2 + \lambda_2 \|PSF \otimes R_{\theta}(y' - b) - y'\|_2^2 \right], \quad (14)$$

where R_{θ} denotes the network with parameters θ , b represents the estimated noise expectation, and λ_2 denotes the regularization coefficient. Here, the learnable bias b serves as an explicit estimator of the noise expectation μ , transforming the ill-posed biased reconstruction problem into a physically consistent optimization task. Under the same imaging system, consecutive observations share consistent noise bias statistics, allowing the global bias b to be estimated through multi-frame joint optimization. Although b is formally a free parameter and could theoretically degenerate into a trivial solution in single-frame optimization, in practice, such degeneration increases reconstruction error across all frames and is therefore naturally avoided in multi-frame joint optimization. Moreover, the reconstruction network R_{θ} is trained on the bias-corrected input $y' - b$, with reconstruction error driving the collaborative update of b and θ , ensuring that b learns the true noise expectation rather than an arbitrary trivial value. Considering both the

shared noise bias across multiple frames and the frequency-domain constraints imposed by defocus blur, the optimal b statistically corresponds to the true noise expectation. As shown in Fig. 1(a), even an accurately restored sharp image, when convolved with the PSF, should not deviate significantly from the observed noisy and blurred image. Motivated by this observation, the regularization term is designed to prevent b from overfitting to an inaccurate PSF by penalizing excessive deviations of the corrected blurry image from the observation. Consequently, this multi-frame joint optimization design is both theoretically and practically sound.

To further reduce the data requirement, we propose pretrain-finetune Physen-Noise2Noise (PF-PN2N), a pretrain–finetune framework. A model is first pretrained on images with similar noise characteristics and then finetuned using a small amount of observations. This strategy enables efficient adaptation to new data distributions, achieving performance comparable to training from scratch with substantially larger datasets.

IV. EXPERIMENT

A. Settings and details

SN2N implementation. The proposed SN2N in this paper adopts a U-Net architecture with symmetric skip connections. The network consists of six encoding blocks and five decoding blocks, all implemented using fully convolutional operations.

All convolutional layers employ 3×3 kernels with a stride of 1 and padding 1. Downsampling is performed using 2×2 max pooling operations with a stride of 2, while upsampling is achieved through transposed convolutions with a stride of 2, padding 1, and output padding 1. The network uses ReLU activation functions in all intermediate layers, with a LeakyReLU activation (negative slope=0.1) in the final output layer. All convolutional and transposed convolutional layers are initialized using Kaiming Normal initialization, with bias terms set to zero. The model implementation is consistent with [41]. The analysis of the hyperparameters of this model can be found in [2], [41], where it has been discussed in detail in these works.

Bias-DeblurNet implementation. The proposed deep neural network, Bias-DeblurNet, follows a U-Net-style encoder-decoder architecture with symmetric skip connections. The network comprises five encoding blocks and four decoding blocks, all implemented using fully convolutional operations. Each convolutional layer is followed by batch normalization to ensure stable training.

Prior to feature extraction, the input is preprocessed by subtracting a learnable spatial bias. This bias term has a shape of $[1, W, H, 1]$, where W and H are the input width and height, respectively. This spatially varying bias parameter is replicated across the batch dimension and optimized jointly with other network parameters during training.

All convolutional layers use 3×3 kernels with a stride of 1 and 'SAME' padding. Downsampling is performed via 2×2 max pooling with 'SAME' padding, while upsampling is carried out using transposed convolutions with a stride of 2. The network primarily employs Softplus activation functions,

TABLE I
ABLATION STUDY RESULTS ON SIMULATE DATASETS.

PSF	T1		T2		T3		T4	
	PSNR \uparrow	SSIM \uparrow	PSNR \uparrow	SSIM \uparrow	PSNR \uparrow	SSIM \uparrow	PSNR \uparrow	SSIM \uparrow
1	26.78	0.9258	15.11	0.3009	29.59	0.9175	30.25	0.9298
2	23.60	0.8638	17.11	0.3986	29.75	0.9108	29.81	0.9157
3	24.81	0.8548	17.43	0.4050	26.54	0.8302	27.86	0.8627
4	22.18	0.7301	16.25	0.3662	23.87	0.7045	26.52	0.7894
5	18.72	0.5054	17.05	0.3997	22.33	0.5977	23.79	0.6786

with ReLU used in specific initial layers. The final output layer uses a Sigmoid activation function to generate normalized estimates.

The model is optimized using the Adam optimizer with differential learning rates: 0.01 for the bias parameters and 0.0001 for all other network parameters. Training proceeds for 5,000 to 10,000 steps. The model was implemented in Python 3.8 using TensorFlow 2.4.0, with GPU acceleration (NVIDIA GeForce RTX 3090) on a Linux system.

Methods included for comparison. In the field of deblurring, numerous outstanding studies have been proposed, each addressing distinctly different problem characteristics. For comparison, we selected the following representative methods: UNID [24], SSI [23], and RLSN2N [2], which are open-source, self-supervised deep learning-based deblurring methods recently developed for high noise environments. Their research objectives and technical approaches align closely with ours; WD [27] and LRA [28], [29] are classical algorithms that remain widely adopted; and NLR [30] is a non-learning method derived from extensions of classical theories. Methods that are not specifically designed for noisy conditions are not included, as preliminary experiments indicate that they degrade significantly under the considered high-noise settings, making the comparison less meaningful. These methods represent exemplary works under noisy conditions across different technical routes. Comprehensive comparisons with them sufficiently demonstrate the effectiveness and advantages of our proposed method. In all experiments, we tuned the hyperparameters of each method to ensure a fair comparison and optimal performance.

B. Ablation study

We constructed a benchmark using five real PSFs, corresponding to different apertures and defocus levels, all measured in the laboratory. All PSFs are shown in the appendix. For each PSF, ten representative images were selected from the Imagenet [62] and CVG-UGR [63] datasets. These images were degraded via convolution with the PSFs and further corrupted by complex biased noise according to Eq. (15):

$$n \sim \mathcal{P}(\mu_p) + \mathcal{N}(\mu_n, \sigma^2), \quad (15)$$

where n denotes the per-pixel noise, \mathcal{P} is a Poisson distribution, and \mathcal{N} is a normal distribution. The parameters μ_n ,

TABLE II
MODEL CONFIGURATION. \checkmark INDICATES THAT THE MODULE IS INCLUDED.

Configuration	SN2N initialization	Bias-adaptive	DeblurNet
T1	\checkmark	\times	\times
T2	\times	\checkmark	\checkmark
T3	\checkmark	\times	\checkmark
T4	\checkmark	\checkmark	\checkmark

μ_p , and σ^2 are pixel-dependent, determined by the spatial coordinates (x, y) as defined in Eqs. (16)–(18):

$$\mu_p = 0.001 \cdot \left(\frac{x}{4}\right)^2 + 0.02 \cdot y + 2, \quad (16)$$

$$\mu_n = 0.01 \cdot x + 0.01 \cdot y + 2, \quad (17)$$

$$\sigma^2 \sim U(20, 50), \quad (18)$$

where U denotes a uniform distribution. In real-world imaging, noise variance is signal-dependent, whereas noise bias remains stable over short intervals [26]. We model the bias as shared across frames and draw variance σ^2 independently per image. We conducted ablation study on this benchmark, with results presented in Fig. 3(b), Table I, and Table II.

As can be seen from Fig. 3(b), Table I, and Table II, each module plays a critical role. The deblurring method with a bias term significantly outperforms others without the bias term. This improvement can be attributed to the fact that incorporating a bias term effectively eliminates the expectation of the biased noise distribution in the blurred image during the deblurring process. This phenomenon validates the effectiveness of our proposed method and the rationality of our theoretical conclusions in Section III-B.

C. Stability analysis

Robustness to image noise. To further validate the robustness of PN2N, we conducted deblurring experiments on a simulated dataset under diverse noise conditions. The configuration of noise conditions is detailed in Table III, and the experimental results are summarized in Table IV and Fig. 3(c). All evaluation metrics consistently demonstrate the strong robustness of PN2N.

Traditional methods often exhibit a bias toward specific noise types, achieving satisfactory performance only when the noise aligns with their underlying assumptions. For instance, Wiener filtering performs well under Gaussian noise, while Richardson–Lucy-based methods (LRA, RLSN2N) excel in high Poisson noise scenarios. However, their performance degrades significantly when dealing with mixed and complex bias noise. Recent noise-robust deblurring approaches, such as UNID and SSI, have demonstrated improved robustness across various noise conditions compared to traditional methods. Nevertheless, PN2N achieves performance that is either superior to or on par with existing methods under almost all

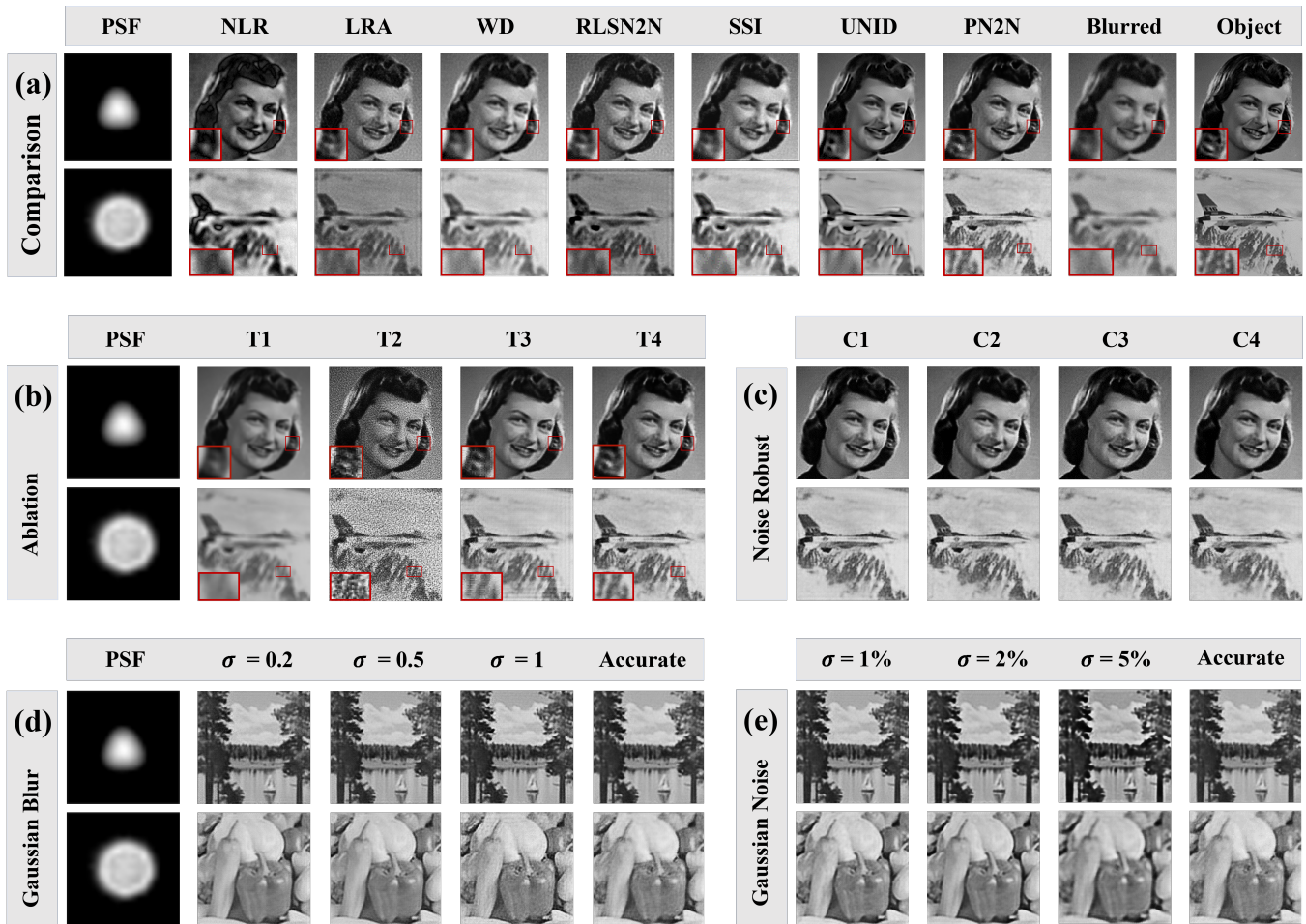


Fig. 3. (a) Comparison of different methods on simulated data. (b) Ablation study on simulated data. (c) Performance comparison of PN2N under various noise conditions. (d) Comparison of PN2N with and without PSF mismatch. (e) Comparison of PN2N with accurate and inaccurate PSF due to noise. The original images used in this figure are from [62], [63].

tested noise conditions and PSFs. Specifically, PN2N performs comparably to existing methods only in the pure Poisson noise scenario, while it outperforms all alternatives under all other noise conditions.

Robustness to PSF uncertainty. To evaluate the robustness of the proposed method against inaccuracies in the point spread function (PSF), we conduct defocus deblurring experiments on simulated datasets using two PSFs with distinct defocus levels—one corresponding to mild defocus and the other to severe defocus. Both PSFs are intentionally perturbed to emulate common errors encountered in practical PSF estimation.

Two types of degradation are introduced. (i) Gaussian blur with varying standard deviations is applied to the ground-truth PSF to simulate defocus mismatch and modeling inaccuracies, resulting in PSF mismatches between the assumed and actual blurs; (ii) additive Gaussian noise at different levels is added to the PSF to replicate measurement noise arising from sensor limitations or calibration errors during PSF acquisition.

Table V presents robust reconstruction results with or without regularization. In the case of an accurate PSF, for mild blur with PSF 3, the inclusion of regularization has little effect on

performance. However, under severe blur with PSF 4, even with the correct PSF, regularization leads to improved results, as the significant loss of high-frequency details makes the bias parameter prone to overfitting, which regularization helps to mitigate.

Table V, Fig. 3(d), and Fig. 3(e) present robust reconstruction results. As the degradation level increases, the following trends are observed: under mild blur, the algorithm experiences a slight performance drop but remains robust; under severe blur, minor degradations still yield acceptable performance, but excessive degradation leads to poor reconstruction quality. In contrast, regularization helps maintain robustness even in cases of substantial PSF mismatch. Overall, while the performance of PN2N degrades to some extent under inaccurate PSFs, it remains robust across a variety of degradation scenarios.

D. Quantitative evaluation with simulation dataset

We compared the deblurring performance of various methods on the benchmark in Section IV-B. The deblurring results are shown in Fig. 3(a) and Table IV.

TABLE III
CONFIGURATION UNDER DIFFERENT NOISE CONDITIONS IN METHODS COMPARISON.

Condition	μ	σ	Distribution
C1	–	$\sigma^2 = 100$	$\mathcal{N}(0, \sigma^2)$
C2	$\mu = 15$	–	$\mathcal{P}(\mu)$
C3	$\mu_p = 0.001 \cdot (x/4)^2 + 0.02 \cdot y + 2, \mu_n = 0.01 \cdot x + 0.01 \cdot y + 2$	$\sigma^2 \sim U(20, 50)$	$\mathcal{P}(\mu_p) + \mathcal{N}(\mu_n, \sigma^2)$
C4	$\mu_n = 0.001 \cdot (x/4)^2 + 0.02 \cdot y + 2, \mu_p = 0.01 \cdot x + 0.01 \cdot y + 2$	$\sigma^2 \sim U(20, 50)$	$\mathcal{P}(\mu_p) + \mathcal{N}(\mu_n, \sigma^2)$

TABLE IV
NOISE ROBUSTNESS COMPARISON OF PN2N AND COMPARATIVE METHODS.

	PSF	NLR		LRA		WD		SSI		UNID		RL-SN2N		PN2N	
		PSNR \uparrow	SSIM \uparrow	PSNR \uparrow	SSIM \uparrow	PSNR \uparrow	SSIM \uparrow	PSNR \uparrow	SSIM \uparrow	PSNR \uparrow	SSIM \uparrow	PSNR \uparrow	SSIM \uparrow	PSNR \uparrow	SSIM \uparrow
C1	3	16.52	0.6589	24.21	0.7904	27.10	0.8560	24.97	0.7861	24.60	0.8562	24.50	0.8100	27.78	0.8586
	4	17.55	0.6176	21.53	0.6902	24.09	0.7596	21.91	0.6715	21.89	0.7387	18.85	0.6926	26.14	0.7828
C2	3	16.78	0.6916	25.93	0.8624	27.30	0.8692	25.57	0.8489	24.72	0.8685	26.08	0.8713	27.69	0.8703
	4	17.78	0.6478	22.23	0.7642	24.19	0.7741	22.50	0.7280	21.97	0.7440	22.56	0.7611	26.06	0.7820
C3	3	16.82	0.6725	24.00	0.7788	26.29	0.8435	25.65	0.8151	24.83	0.8541	24.07	0.8006	27.86	0.8627
	4	17.88	0.6261	20.82	0.6780	23.40	0.7463	22.43	0.6868	22.17	0.7538	19.47	0.7038	26.52	0.7894
C4	3	16.73	0.6900	25.96	0.8823	27.30	0.8803	25.75	0.8135	24.63	0.8519	25.45	0.8783	27.88	0.8857
	4	17.83	0.6296	21.58	0.6806	23.49	0.7465	22.37	0.6807	22.26	0.7467	18.75	0.6861	25.25	0.7509

TABLE V
ROBUSTNESS OF PN2N TO PSF MISMATCH AND MEASUREMENT NOISE.

Regularization	PSF	Metric	Gaussian blur (σ)				Gaussian noise level (σ)			
			Accurate	0.2	0.5	1	Accurate	1%	2%	5%
×	3	PSNR \uparrow	27.86	27.52	27.08	26.70	27.86	26.97	24.92	21.99
		SSIM \uparrow	0.8627	0.8514	0.8400	0.8262	0.8627	0.8376	0.7910	0.7315
×	4	PSNR \uparrow	26.52	25.15	25.02	24.24	26.52	25.28	25.24	23.82
		SSIM \uparrow	0.7894	0.7399	0.7677	0.7199	0.7894	0.7537	0.7603	0.7444
✓	3	PSNR \uparrow	27.70	27.84	27.78	26.52	27.70	27.78	26.24	22.48
		SSIM \uparrow	0.8614	0.8599	0.8407	0.8305	0.8614	0.8588	0.8607	0.8193
✓	4	PSNR \uparrow	26.21	26.16	25.96	25.28	26.21	25.48	25.52	24.14
		SSIM \uparrow	0.7937	0.7661	0.7652	0.7648	0.7937	0.7765	0.7814	0.7625

TABLE VI
PERFORMANCE COMPARISON OF DIFFERENT METHODS ON SIMULATION DATASET

	NLR		LRA		WD		SSI		UNID		RL-SN2N		PN2N	
	PSF	PSNR \uparrow	SSIM \uparrow	PSNR \uparrow	SSIM \uparrow	PSNR \uparrow	SSIM \uparrow	PSNR \uparrow	SSIM \uparrow	PSNR \uparrow	SSIM \uparrow	PSNR \uparrow	SSIM \uparrow	PSNR \uparrow
1	15.51	0.6560	23.17	0.7243	28.62	0.8590	23.23	0.7770	27.37	0.9161	26.62	0.8422	30.25	0.9298
2	19.47	0.7154	23.10	0.7521	26.34	0.8333	25.69	0.8561	23.36	0.8552	25.45	0.7826	29.81	0.9157
3	16.82	0.6725	24.00	0.7788	26.29	0.8435	25.65	0.8151	24.83	0.8541	24.07	0.8006	27.86	0.8627
4	17.88	0.6261	20.82	0.6780	23.40	0.7463	22.43	0.6868	22.17	0.7538	19.47	0.7038	26.52	0.7894
5	18.42	0.5054	15.05	0.3828	18.61	0.5142	16.25	0.3587	18.16	0.4836	15.27	0.4438	23.79	0.6786

In quantitative comparisons of different non-independent and identically distributed noise suppression methods, the proposed approach consistently achieves the best performance across all experimental settings. Under mild defocus blur, the performance gap among methods is relatively small, with UNID demonstrating competitive results. However, as the defocus blur intensifies, high-frequency details are progressively smoothed out, and noise introduces more severe perturbations in the high-frequency domain, substantially degrading deblurring performance. Under such conditions, the complex

characteristics of biased noise pose significant challenges to existing methods. UNID leverages model uncertainty via Monte Carlo Dropout (MCdropout) to enhance noise robustness, but it tends to conflate high-frequency details with noise, thereby impairing restoration quality. SSI relies on mask-based denoising and struggles to handle spatially correlated noise. Traditional physics-based iterative methods (WD, LRA, NLR) suffer from significant performance degradation in such complex biased noise environments. RLSN2N also fails to model biased noise due to its conventional iterative deblurring

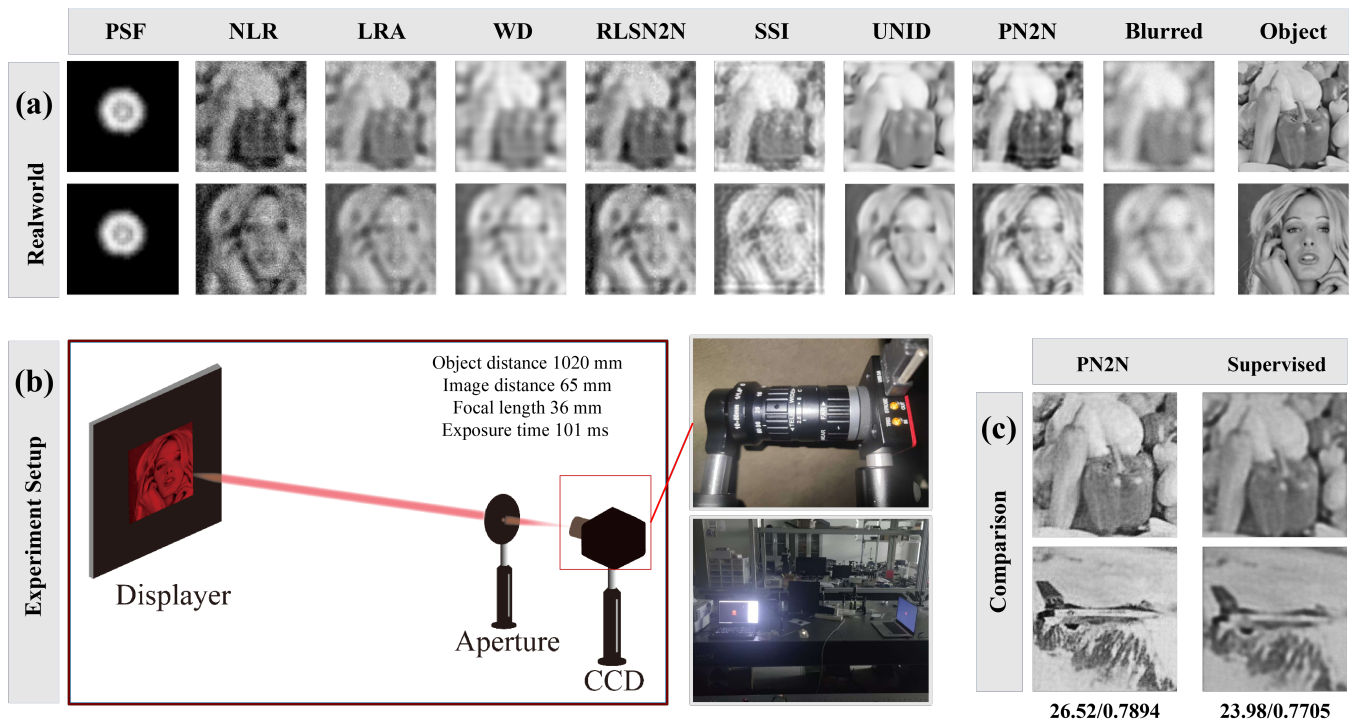


Fig. 4. (a) Comparison of different methods on real experimental data. (b) Experimental setup and equipment for real-world validation. (c) A simple comparison of supervised learning and PN2N under PSF 4 with the same network. Values shown on the images indicate PSNR / SSIM. The original images used in this figure are from [62], [63].

algorithms. In contrast, PN2N consistently delivers the best overall performance across all scenarios. These results validate the theory presented in Section III-B.

E. Experimental evaluation with captured images

We conducted experiments using the optical setup shown in Fig. 4(b). A color camera (CS165MU-M) coupled with a zoom lens (LBMV1236M) was employed under red light illumination, with a fixed 1 mm radius small-aperture diaphragm mounted in front of the lens. Target images were presented on a laptop display. The PSF was acquired through defocused imaging.

Our experimental procedure comprised three steps. First, a test image was displayed on a black background, and the lens focal length was adjusted to achieve the target defocus level. Second, while keeping the optical setup unchanged, the test image was replaced by a pinpoint light source (a single bright pixel on a black background) to image the PSF. Finally, the original test image was displayed again and captured. Continuous image capture was controlled via a Python script. The main parameters were set as follows: object distance 1020 mm, image distance 65 mm, focal length 36 mm, and exposure time 101 ms.

We captured 10 target images selected from the Imagenet [62] and CVG-UGR [63] datasets, with 400 consecutive frames sampled per target, yielding a total of 4000 single images. These frames were paired to form 2000 image pairs. The entire dataset was randomly divided into two subsets:

TABLE VII
COMPARISON OF THE RESULTS OF DIFFERENT METHODS ON DEFOCUSED EXPERIMENT.

	PN2N	UNID	SSI	WD	LRA	NLR	RL-SN2N
PSNR \uparrow	18.16	18.67	16.96	17.66	17.18	15.13	16.28
SSIM \uparrow	0.5875	0.5654	0.4621	0.4473	0.4444	0.2911	0.4346

TABLE VIII
COMPARISON OF THE RESULTS ON PRETRAIN-FINETUNE PARADIGM. T STANDS FOR DIRECT TRAINING, PF STANDS FOR PRETRAIN-FINETUNE PARADIGM, AND PRETRAIN STANDS FOR PRETRAINING ONLY.

	Pretrain	T 100	PF 100	T 300	PF 300	T 1000
PSNR \uparrow	16.63	18.13	18.24	18.14	18.52	18.16
SSIM \uparrow	0.3891	0.5488	0.5647	0.5718	0.5878	0.5875

- **Set A** (5 targets, 1000 pairs) was used for deblurring using the PF-PN2N method.
- **Set B** (the remaining 5 targets, 1000 pairs) was utilized to pre-train the SN2N model.

PN2N was evaluated on both **Set A** and **Set B**. For PF-PN2N, we applied the method to a subset of 100 image pairs from **Set A**, leveraging the SN2N model pre-trained on **Set B**.

We compared the different methods, including tests on PN2N and PF-PN2N. Results are presented in Fig. 4(a) and Table VII. PN2N outperforms all approaches in terms of SSIM. Although its PSNR is slightly lower than that of UNID [24], this is due to UNID's tendency to over-smooth images,

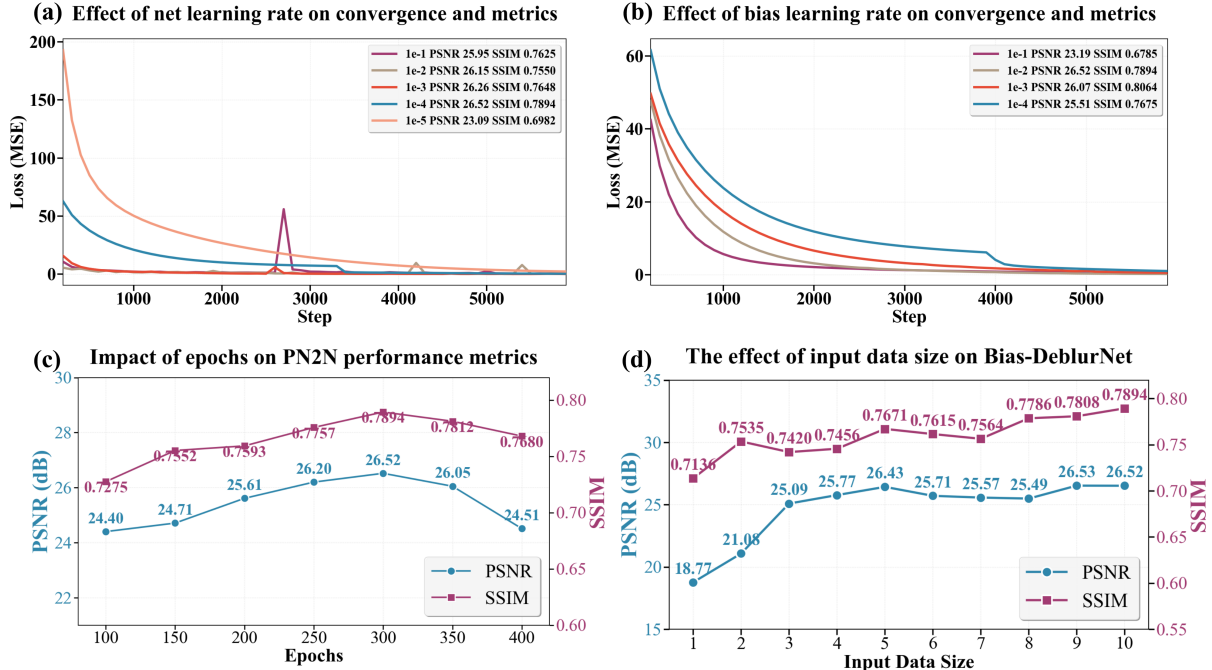


Fig. 5. (a) illustrates the effect of the primary network learning rate on convergence and deblurring performance, while (b) shows the impact of the learnable bias learning rate on convergence and deblurring performance. (c) presents the final deblurring performance under different training epochs, and (d) demonstrates the effect of the self-supervised training data size on the deblurring performance of Bias-DeblurNet.

leading to noticeable artifacts. PF-PN2N also matches PN2N performance on a small dataset (Table VIII). Overall, PN2N outperforms all existing alternatives.

F. Hyperparameter analysis of PN2N

PSF 4 represents a relatively severe point spread function that leads to noticeable blurring, yet it does not cause extreme degradation or complete loss of structural information. Consequently, it serves as a suitable benchmark for evaluating defocus deblurring performance under challenging yet realistic conditions. We conducted systematic experiments to investigate the impact of key hyperparameters of PN2N under the PSF4 setting. The results are shown in Fig. 5.

We first examined the effect of the main network learning rate. With the bias term learning rate fixed at 1×10^{-2} and training for 6,000 steps, the main network learning rate was varied from 1×10^{-1} to 1×10^{-5} . A comparison of convergence curves and performance metrics revealed that a learning rate of 1×10^{-4} yields the most stable and effective deblurring performance. Next, we explored the effect of the bias term learning rate. Keeping the main network learning rate at 1×10^{-4} and training for 6,000 steps, the bias term learning rate was varied from 1×10^{-1} to 1×10^{-4} . The results showed that a bias term learning rate of 1×10^{-2} achieves the optimal balance between convergence speed and reconstruction quality. Due to the self-supervised nature of the proposed framework, the network can converge under a wide

range of learning rates. However, the learning rate significantly affects the reconstruction fidelity. Larger learning rates tend to yield faster convergence but may lead to suboptimal fine details, while smaller learning rates improve reconstruction precision at the cost of slower convergence.

We also investigated the effect of the SN2N initialization step. With the bias term learning rate set to 1×10^{-2} , the main network learning rate at 1×10^{-4} , and training for 6,000 steps, the SN2N initialization step was varied from 100 to 400. Comparative metric analysis indicated that initialization at step 300 yields the best deblurring performance. The SN2N initialization stage plays a critical role in stabilizing early training. Insufficient initialization leads to unstable representations, while excessive iterations may cause the network to overfit the noisy observations. An intermediate number of steps provides a balanced initialization for subsequent joint optimization.

The influence of training data size for Bias-DeblurNet was further evaluated. Under the same fixed configuration (bias term learning rate 1×10^{-2} , main network learning rate 1×10^{-4} , 6,000 steps), the number of training images was varied from 1 to 10. When only a single training image is used, the reconstruction quality is limited due to insufficient statistical information. With a small number of images, the performance remains unstable. Once the number of training samples reaches around five, the reconstruction quality becomes significantly more stable and gradually saturates as more data are introduced.

Overall, these results indicate that the proposed method exhibits stable performance within a reasonable range of hyperparameters and does not require delicate tuning.

V. DISCUSSION AND LIMITATION

Our core contribution lies in enabling robust defocus deblurring under challenging low-light and long-exposure conditions. In such scenarios, noise is often biased and deviates from the commonly assumed zero-mean distribution, yet this factor is largely overlooked in existing degradation models. To address this gap, we explicitly model biased noise and incorporate it into the restoration process. Furthermore, we exploit the optimization stagnation phenomenon caused by physical model mismatch to enable noise bias correction without requiring clean reference images. This mechanism allows the network to progressively compensate for bias during self-supervised optimization, thereby improving deblurring performance under severe degradation conditions.

Our method does not rely on generative models to provide additional image priors. Instead, it leverages an autoregressive learning mechanism that naturally suits the ill-posed nature of this problem. It should be noted that under extreme blur conditions, our approach struggles to recover high-frequency details as generative models do, resulting in certain limitations in detail restoration. However, its core advantages include achieving favorable restoration without requiring training data and demonstrating performance comparable to that of non-generative end-to-end learning under the same network architecture, as illustrated in Fig. 4(c).

As a nonblind defocus deblurring method, our framework cannot simultaneously perform point spread function estimation and image deblurring. Although we have validated its robustness to inaccurate PSF under the challenging degradation scenario of complex biased noise, achieving blind deblurring remains a limitation and a key direction for future research.

TABLE IX
COMPARISON OF STEP NUMBER AND RUNTIME OF METHODS ON PSF 4.

Method	Step Number	Runtime	PSNR	SSIM
NLR	25	2.0 s	17.88	0.6261
LRA	20	1.6 s	20.82	0.6780
WD	1	1 ms	23.40	0.7463
SSI	8000	10.8 min	22.43	0.6868
UNID	10000	3.5 min	22.17	0.7538
PN2N	6000	7.5 min	26.52	0.7894
RL-SN2N	20	15 min	19.47	0.7038

Regarding computational efficiency, as a self-supervised method, our framework cannot achieve the high-speed inference of trained supervised learning approaches. This represents both an advantage (no training required) and a current limitation (difficulty in real-time processing). Nevertheless, compared to similar methods, our deblurring approach maintains competitive efficiency as shown in Table IX. Future work will focus on further accelerating the autoregressive learning process to meet real-time processing requirements.

VI. CONCLUSION AND FUTURE WORK

We propose Physen-Noise2Noise, a novel self-supervised deep learning deblurring framework specifically designed for low-light, long-exposure, and defocused scenarios. This method incorporates frequency-domain constraints based on physical models and utilizes multi-frame data continuously captured within a short time interval. Through learnable noise bias, it integrates the initialization process of SN2N with the autoregressive learning mechanism of Bias-DeblurNet, ultimately achieving excellent performance in deblurring tasks under complex biased noise distributions. The framework effectively handles complex biased noise that is position-dependent, varies pixel-wise, and follows mixture distributions, under the least restrictive assumptions about noise characteristics. Its pretrain-finetune paradigm enhances model robustness and computational efficiency even with sparse training data. Future work will address current limitations in PSF estimation accuracy and optimize computational speed for real-time processing.

ACKNOWLEDGEMENT

The authors acknowledge the support of National Natural Science Foundation of China (NSFC) under Grant Number 12571470, 12271526 and 62275077. The work was supported by the Major Scientific and Technological Innovation Platform Project of Hunan Province (2024JC1003) and High-level Talent Research Start-up Project Funding of Henan Academy of Sciences (Project N0.232019024). Part of this work was carried out in part using computing resources at the High Performance Computing Center of Central South University.

APPENDIX

PROOF OF THE FREQUENCY-DOMAIN CONSTRAINTS

Proof. [of Proposition 1] The theoretical analysis of the PSF convolution in the imaging model is initially conducted under pristine, noise-free conditions.

According to the imaging model $PSF \otimes x$, \mathcal{V} is also a subspace of the object image space \mathcal{O} . \mathcal{O} and \mathcal{I} are energy-limited (finite energy in the frequency domain) due to physical constraints. It implies:

$$\forall x \in \mathcal{I}, \int_{\Omega} |F_x(\omega)|^2 d\omega < \infty, \quad (19)$$

where $F_x(\omega)$ is the Fourier transform of the x in \mathcal{I} .

Scenario 1 Assume the PSF satisfies condition (1), and let \mathcal{V} be a subspace of the image space \mathcal{I} . Since the PSF satisfies condition S1, there exists at least one frequency component ξ such that $|F_p(\xi)| = 0$.

Neglecting noise and applying the Fourier transform to

$$y = PSF \otimes x, \quad (20)$$

we obtain the frequency-domain expression:

$$|F_y(\omega)| = |F_p(\omega)| \cdot |F_x(\omega)|, \quad (21)$$

where $F_y(\omega)$ is the Fourier transform of the y in \mathcal{V} . Specifically, at frequency ξ :

$$|F_y(\xi)| = |F_p(\xi)| \cdot |F_x(\xi)| = 0 \cdot |F_x(\xi)| = 0. \quad (22)$$

Therefore, the Fourier transform of every element in \mathcal{V} is zero at ξ .

Now, consider an element $i \in \mathcal{I}$. Its Fourier transform $F_i(\omega)$ satisfies $|F_i(\xi)| \neq 0$. This contradicts Eq. (22), implying that $i \notin \mathcal{V}$. Consequently, there exists an element $i \in \mathcal{I}$ such that $i \notin \mathcal{V}$, which establishes that \mathcal{V} is a strict subset of \mathcal{I} . This proves that \mathcal{V} is a proper subspace of \mathcal{I} .

Scenario 2 The second scenario is when the PSF follows condition (2). Since the PSF exhibits high-frequency decay, $F_p(\omega)$ satisfies Eq. (4).

We now proceed to demonstrate that \mathcal{V} constitutes a proper subspace of \mathcal{I} . To ensure \mathcal{I} is certainly energy-limited as stated in Eq. (19), the following must hold:

$$\forall y \in \mathcal{V}, \int_{\Omega} \left(\frac{|F_y(\omega)|^2}{|F_p(\omega)|^2} \right) d\omega = \int_{\Omega} |F_x(\omega)|^2 d\omega < \infty. \quad (23)$$

Then, the observed image space \mathcal{V} satisfies:

$$\mathcal{V} \subseteq \left\{ y \in \mathcal{I} \mid \int_{\Omega} \left(\frac{|F_y(\omega)|^2}{|F_p(\omega)|^2} \right) d\omega < \infty \right\} := \mathcal{V}^*. \quad (24)$$

The complement of \mathcal{V}^* is non-empty. Indeed, it is always possible to construct an $F_y(\omega)$ that obeys Eq. (19) such that Eq. (23) fails. Specifically, by defining:

$$F_y(\omega) = \frac{F_p(\omega)}{1 + |\omega|}, \quad (25)$$

and noting that:

$$1 + |\omega| \geq 1 > 0, \quad \forall \omega \in \Omega, \quad (26)$$

we obtain:

$$|F_y(\omega)|^2 = \frac{|F_p(\omega)|^2}{|1 + |\omega||^2} \leq |F_p(\omega)|^2. \quad (27)$$

Since the PSF is also an image (i.e., $PSF \in \mathcal{I}$), it satisfies Eq. (19). Hence,

$$\int_{\Omega} |F_y(\omega)|^2 d\omega \leq \int_{\Omega} |F_p(\omega)|^2 d\omega < \infty, \quad (28)$$

which immediately implies $y \in \mathcal{I}$. Now consider the ratio:

$$\frac{|F_y(\omega)|^2}{|F_p(\omega)|^2} = \frac{1}{(1 + |\omega|)^2}. \quad (29)$$

Switching to polar coordinates ($|\omega| = r$, $d\omega = r dr d\theta$):

$$\int_{\Omega} \frac{1}{(1 + |\omega|)^2} d\omega = 2\pi \int_0^{\infty} \frac{r}{(1 + r)^2} dr. \quad (30)$$

Let $t = 1 + r$, then $r = t - 1$ and $dr = dt$. The integral becomes:

$$\int_0^{\infty} \frac{r}{(1 + r)^2} dr = \int_1^{\infty} \frac{t-1}{t^2} dt = \left[\ln t + \frac{1}{t} \right]_1^{\infty}. \quad (31)$$

As $t \rightarrow \infty$, $\ln t \rightarrow \infty$, while $\frac{1}{t} \rightarrow 0$, so the integral diverges. Therefore,

$$\int_{\Omega} \frac{1}{(1 + |\omega|)^2} d\omega = \infty. \quad (32)$$

Hence, $F_p(\omega)$ obeys condition (2), $y \in \mathcal{I}$ but leads to the violation of Eq. (23). Combining Eq. (28) and Eq. (32), we can derive that there exists an element $i \in \mathcal{I}$ such that $i \notin \mathcal{V}$, which establishes that \mathcal{V} is a proper subspace of \mathcal{I} .

In summary, the observed image space \mathcal{V} is a proper subspace of \mathcal{I} :

$$\mathcal{V} \subsetneq \mathcal{I} = \mathcal{O}. \quad (33)$$

□

THE PSF IN EXPERIMENTS

To comprehensively evaluate the performance of our proposed non-blind defocus deblurring method, we incorporate PSFs corresponding to various defocus levels and aperture shapes in our experiments. All the PSFs used in our experiments are shown in Fig. 6.

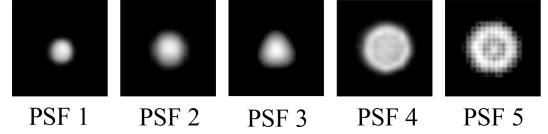


Fig. 6. PSF used in the experiment.

REFERENCES

- [1] S. Ai and J. Kwon, "Extreme low-light image enhancement for surveillance cameras using attention u-net," *Sensors*, vol. 20, no. 2, p. 495, 2020.
- [2] L. Qu, S. Zhao, Y. Huang, X. Ye, K. Wang, Y. Liu, X. Liu, H. Mao, G. Hu, W. Chen *et al.*, "Self-inspired learning for denoising live-cell super-resolution microscopy," *Nature Methods*, vol. 21, no. 10, pp. 1895–1908, 2024.
- [3] J. Tao, J. Wang, P. Zhang, J. Zhang, K.-L. Yung, and W. H. Ip, "Legan: A low-light image enhancement generative adversarial network for industrial internet of smart-cameras," *Internet of Things*, vol. 25, p. 101054, 2024.
- [4] G. E. Healey and R. Kondepudy, "Radiometric ccd camera calibration and noise estimation," *IEEE Transactions on Pattern Analysis and Machine Intelligence*, vol. 16, no. 3, pp. 267–276, 2002.
- [5] H. Tian, *Noise analysis in CMOS image sensors*. stanFord university, 2000.
- [6] M. Konnik and J. Welsh, "High-level numerical simulations of noise in ccd and cmos photosensors: review and tutorial," *arXiv preprint arXiv:1412.4031*, 2014.
- [7] P. Chatterjee, N. Joshi, S. B. Kang, and Y. Matsushita, "Noise suppression in low-light images through joint denoising and demosaicing," in *CVPR 2011*. IEEE, 2011, pp. 321–328.
- [8] Q. Jin, G. Facciolo, and J.-M. Morel, "A review of an old dilemma: Demosaicing first, or denoising first?" in *proceedings of the IEEE/CVF conference on computer vision and pattern recognition workshops*, 2020, pp. 514–515.
- [9] S. H. Park, H. S. Kim, S. Lancel, M. Parmar, and B. A. Wandell, "A case for denoising before demosaicing color filter array data," in *2009 Conference Record of the Forty-Third Asilomar Conference on Signals, Systems and Computers*. IEEE, 2009, pp. 860–864.
- [10] W. Lee, S. Son, and K. M. Lee, "Ap-bsn: Self-supervised denoising for real-world images via asymmetric pd and blind-spot network," in *Proceedings of the IEEE/CVF Conference on Computer Vision and Pattern Recognition*, 2022, pp. 17725–17734.

- [11] K. Zhang, W. Zuo, Y. Chen, D. Meng, and L. Zhang, "Beyond a gaussian denoiser: Residual learning of deep cnn for image denoising," *IEEE transactions on image processing*, vol. 26, no. 7, pp. 3142–3155, 2017.
- [12] J. Liang, J. Cao, G. Sun, K. Zhang, L. Van Gool, and R. Timofte, "Swinir: Image restoration using swin transformer," in *Proceedings of the IEEE/CVF international conference on computer vision*, 2021, pp. 1833–1844.
- [13] H. Chen, J. Gu, Y. Liu, S. A. Magid, C. Dong, Q. Wang, H. Pfister, and L. Zhu, "Masked image training for generalizable deep image denoising," in *Proceedings of the IEEE/CVF Conference on Computer Vision and Pattern Recognition*, 2023, pp. 1692–1703.
- [14] S. Herbreteau, E. Moebel, and C. Kervrann, "Normalization-equivariant neural networks with application to image denoising," *Advances in Neural Information Processing Systems*, vol. 36, pp. 5706–5728, 2023.
- [15] R. Li, C. Liu, Z. Wang, Y. Du, J. Yang, L. Bao, and H. Sun, "From synthetic to real: A calibration-free pipeline for few-shot raw image denoising," in *Proceedings of the IEEE/CVF Conference on Computer Vision and Pattern Recognition*, 2024, pp. 1106–1114.
- [16] J. Dong, S. Roth, and B. Schiele, "Learning spatially-variant map models for non-blind image deblurring," in *Proceedings of the IEEE/CVF conference on computer vision and pattern recognition*, 2021, pp. 4886–4895.
- [17] Y. Sanghvi, A. Gnanasambandam, and S. H. Chan, "Photon limited non-blind deblurring using algorithm unrolling," *IEEE Transactions on Computational Imaging*, vol. 8, pp. 851–864, 2022.
- [18] Z. Zhang, Y. Cheng, J. Suo, L. Bian, and Q. Dai, "Infwide: Image and feature space wiener deconvolution network for non-blind image deblurring in low-light conditions," *IEEE Transactions on Image Processing*, vol. 32, pp. 1390–1402, 2023.
- [19] J. Dong, S. Roth, and B. Schiele, "Deep wiener deconvolution: Wiener meets deep learning for image deblurring," *Advances in Neural Information Processing Systems*, vol. 33, pp. 1048–1059, 2020.
- [20] D. Gong, Z. Zhang, Q. Shi, A. Van Den Hengel, C. Shen, and Y. Zhang, "Learning deep gradient descent optimization for image deconvolution," *IEEE transactions on neural networks and learning systems*, vol. 31, no. 12, pp. 5468–5482, 2020.
- [21] Y. Kageyama, M. Isogawa, D. Iwai, and K. Sato, "Prodebnet: projector deblurring using a convolutional neural network," *Opt. Express*, vol. 28, no. 14, pp. 20391–20403, Jul 2020. [Online]. Available: <https://opg.optica.org/oe/abstract.cfm?URI=oe-28-14-20391>
- [22] X.-X. Wei, L. Zhang, and H. Huang, "High-quality blind defocus deblurring of multispectral images with optics and gradient prior," *Opt. Express*, vol. 28, no. 7, pp. 10683–10704, Mar 2020. [Online]. Available: <https://opg.optica.org/oe/abstract.cfm?URI=oe-28-7-10683>
- [23] H. Kobayashi, A. C. Solak, J. Batson, and L. A. Royer, "Image deconvolution via noise-tolerant self-supervised inversion," *arXiv preprint arXiv:2006.06156*, 2020.
- [24] M. Chen, Y. Quan, T. Pang, and H. Ji, "Nonblind image deconvolution via leveraging model uncertainty in an untrained deep neural network," *International Journal of Computer Vision*, vol. 130, no. 7, pp. 1770–1789, 2022.
- [25] S. Wiedemann and R. Heckel, "A deep learning method for simultaneous denoising and missing wedge reconstruction in cryogenic electron tomography," *Nature Communications*, vol. 15, no. 1, p. 8255, 2024.
- [26] H. B. Wach and E. R. Dowski, "Noise modeling for design and simulation of color imaging systems," in *Color and Imaging Conference*, vol. 12. Society of Imaging Science and Technology, 2004, pp. 211–216.
- [27] A. P. Dhawan, R. M. Rangayyan, and R. Gordon, "Image restoration by wiener deconvolution in limited-view computed tomography," *Applied optics*, vol. 24, no. 23, pp. 4013–4020, 1985.
- [28] L. B. Lucy, "An iterative technique for the rectification of observed distributions," *Astronomical Journal*, Vol. 79, p. 745 (1974), vol. 79, p. 745, 1974.
- [29] W. H. Richardson, "Bayesian-based iterative method of image restoration," *Journal of the optical society of America*, vol. 62, no. 1, pp. 55–59, 1972.
- [30] S. Mukherjee and J. Rosen, "Imaging through scattering medium by adaptive non-linear digital processing," *Scientific reports*, vol. 8, no. 1, p. 10517, 2018.
- [31] A. A. Hendriksen, D. M. Pelt, and K. J. Batenburg, "Noise2inverse: Self-supervised deep convolutional denoising for tomography," *IEEE Transactions on Computational Imaging*, vol. 6, pp. 1320–1335, 2020.
- [32] D. Ren, K. Zhang, Q. Wang, Q. Hu, and W. Zuo, "Neural blind deconvolution using deep priors," in *Proceedings of the IEEE/CVF conference on computer vision and pattern recognition*, 2020, pp. 3341–3350.
- [33] X. Tang, X. Zhao, J. Liu, J. Wang, Y. Miao, and T. Zeng, "Uncertainty-aware unsupervised image deblurring with deep residual prior," in *Proceedings of the IEEE/CVF conference on computer vision and pattern recognition*, 2023, pp. 9883–9892.
- [34] X. Qin, Y. Quan, Z. Chen, and H. Ji, "Robust unsupervised deep learning for nonblind image deconvolution with inaccurate kernels," *IEEE Transactions on Neural Networks and Learning Systems*, 2025.
- [35] D. Ulyanov, A. Vedaldi, and V. Lempitsky, "Deep image prior," in *Proceedings of the IEEE conference on computer vision and pattern recognition*, 2018, pp. 9446–9454.
- [36] Z. Wang, Z. Wang, Q. Li, and H. Bilen, "Image deconvolution with deep image and kernel priors," in *Proceedings of the IEEE/CVF International Conference on Computer Vision Workshops*, 2019, pp. 0–0.
- [37] N. G. Nair, R. Yasarla, and V. M. Patel, "Nbd-gap: non-blind image deblurring without clean target images," in *2022 IEEE international conference on image processing (ICIP)*. IEEE, 2022, pp. 3431–3435.
- [38] S. Lim, H. Park, S.-E. Lee, S. Chang, B. Sim, and J. C. Ye, "Cyclegan with a blur kernel for deconvolution microscopy: Optimal transport geometry," *IEEE Transactions on Computational Imaging*, vol. 6, pp. 1127–1138, 2020.
- [39] A. Krull, T.-O. Buchholz, and F. Jug, "Noise2void-learning denoising from single noisy images," in *Proceedings of the IEEE/CVF conference on computer vision and pattern recognition*, 2019, pp. 2129–2137.
- [40] Y. Gal and Z. Ghahramani, "Dropout as a bayesian approximation: Representing model uncertainty in deep learning," in *international conference on machine learning*. PMLR, 2016, pp. 1050–1059.
- [41] J. Lehtinen, J. Munkberg, J. Hasselgren, S. Laine, T. Karras, M. Aittala, and T. Aila, "Noise2noise: Learning image restoration without clean data," *arXiv preprint arXiv:1803.04189*, 2018.
- [42] G.-Z. Yang, P. Burger, D. N. Firmin, and S. Underwood, "Structure adaptive anisotropic image filtering," *Image and Vision Computing*, vol. 14, no. 2, pp. 135–145, 1996.
- [43] H. Takeda, S. Farsiu, and P. Milanfar, "Kernel regression for image processing and reconstruction," *IEEE Transactions on image processing*, vol. 16, no. 2, pp. 349–366, 2007.
- [44] K. Dabov, A. Foi, V. Katkovnik, and K. Egiazarian, "Image denoising by sparse 3-d transform-domain collaborative filtering," *IEEE Transactions on image processing*, vol. 16, no. 8, pp. 2080–2095, 2007.
- [45] L. Zhang, P. Bao, and X. Wu, "Multiscale lmmse-based image denoising with optimal wavelet selection," *IEEE Transactions on circuits and systems for video technology*, vol. 15, no. 4, pp. 469–481, 2005.
- [46] A. Beck and M. Teboulle, "Fast gradient-based algorithms for constrained total variation image denoising and deblurring problems," *IEEE transactions on image processing*, vol. 18, no. 11, pp. 2419–2434, 2009.
- [47] C. Tian, L. Fei, W. Zheng, Y. Xu, W. Zuo, and C.-W. Lin, "Deep learning on image denoising: An overview," *Neural Networks*, vol. 131, pp. 251–275, 2020.
- [48] S. Izadi, D. Sutton, and G. Hamarneh, "Image denoising in the deep learning era," *Artificial Intelligence Review*, vol. 56, no. 7, pp. 5929–5974, 2023.
- [49] M. Elad, B. Kowar, and G. Vaksman, "Image denoising: The deep learning revolution and beyond—a survey paper," *SIAM Journal on Imaging Sciences*, vol. 16, no. 3, pp. 1594–1654, 2023.
- [50] S. Laine, T. Karras, J. Lehtinen, and T. Aila, "High-quality self-supervised deep image denoising," *Advances in neural information processing systems*, vol. 32, 2019.
- [51] T. Pang, H. Zheng, Y. Quan, and H. Ji, "Recorruped-to-recorruped: Unsupervised deep learning for image denoising," in *Proceedings of the IEEE/CVF conference on computer vision and pattern recognition*, 2021, pp. 2043–2052.
- [52] B. Monroy, J. Bacca, and J. Tachella, "Generalized recorruped-to-recorruped: Self-supervised learning beyond gaussian noise," in *Proceedings of the Computer Vision and Pattern Recognition Conference*, 2025, pp. 28155–28164.
- [53] T. Huang, S. Li, X. Jia, H. Lu, and J. Liu, "Neighbor2neighbor: Self-supervised denoising from single noisy images," in *Proceedings of the IEEE/CVF conference on computer vision and pattern recognition*, 2021, pp. 14781–14790.
- [54] Y. Quan, M. Chen, T. Pang, and H. Ji, "Self2self with dropout: Learning self-supervised denoising from single image," in *Proceedings of the*

- IEEE/CVF conference on computer vision and pattern recognition*, 2020, pp. 1890–1898.
- [55] Q. Ma, J. Jiang, X. Zhou, P. Liang, X. Liu, and J. Ma, “Pixel2pixel: A pixelwise approach for zero-shot single image denoising,” *IEEE Transactions on Pattern Analysis and Machine Intelligence*, 2025.
 - [56] J. E. Fröch, P. Chakravarthula, J. Sun, E. Tseng, S. Colburn, A. Zhan, F. Miller, A. Wirth-Singh, Q. A. Tanguy, Z. Han *et al.*, “Beating spectral bandwidth limits for large aperture broadband nano-optics,” *Nature communications*, vol. 16, no. 1, p. 3025, 2025.
 - [57] M. S. Almeida and L. B. Almeida, “Blind and semi-blind deblurring of natural images,” *IEEE Transactions on image processing*, vol. 19, no. 1, pp. 36–52, 2009.
 - [58] J. W. Goodman, *Introduction to Fourier optics*. Roberts and Company publishers, 2005.
 - [59] M. S. Hosseini and K. N. Plataniotis, “Convolutional deblurring for natural imaging,” *IEEE Transactions on Image Processing*, vol. 29, pp. 250–264, 2019.
 - [60] G. D. Boreman, *Modulation transfer function in optical and electro-optical systems*. SPIE press Bellingham, Washington, 2001, vol. 4.
 - [61] F. Wang, Y. Bian, H. Wang, M. Lyu, G. Pedrini, W. Osten, G. Barbas-tathis, and G. Situ, “Phase imaging with an untrained neural network,” *Light: Science & Applications*, vol. 9, no. 1, p. 77, 2020.
 - [62] J. Deng, W. Dong, R. Socher, L.-J. Li, K. Li, and L. Fei-Fei, “Imagenet: A large-scale hierarchical image database,” in *2009 IEEE conference on computer vision and pattern recognition*. Ieee, 2009, pp. 248–255.
 - [63] Computer Vision Group, University of Granada, “Cvg-ugr image database,” <https://ccia.ugr.es/cvg/dbimagenes/>, accessed Jan. 22, 2026.